

1 **Characterizing the evolution of mass flow properties and dynamics through analysis of**
2 **seismic signals: Insights from the 18 March 2007 Mt. Ruapehu lake-breakout lahar**

3

4 Braden Walsh¹, Charline Lormand², Jon Procter³, Glyn Williams-Jones¹

5 ¹Department of Earth Sciences, Simon Fraser University, Burnaby, British Columbia, Canada

6 ²Department of Earth Sciences, University of Durham, Durham, DH1 3LE, UK

7 ³Volcanic Risk Solutions, Institute of Agriculture and Environment, Massey University,

8 Palmerston North, New Zealand

9

10 Corresponding Author: Braden Walsh (braden_walsh@sfu.ca)

11

12 **Abstract**

13 Monitoring for lahars on volcanoes can be challenging due to the ever-changing landscape
14 which can drastically transform the properties and dynamics of the flow. These changes to the
15 flows require the need for detection strategies and risk assessment that are tailored not only
16 between different volcanoes, but at different distances along flow paths as well. Being able to
17 understand how a flow event may transform in time and space along the channel is of utmost
18 importance for hazard management. While visual observations and simple measuring devices in
19 the past have shown how lahars transform along the flow path, these same features for the

20 most part have not been described using seismological methods. On 18 March 2007 Mt.
21 Ruapehu produced the biggest lahar in New Zealand in over 100 years. At 23:18 UTC the tephra
22 dam holding the Crater Lake water back collapsed causing 1.3×10^6 m³ of water to flow out and
23 rush down the Whangaehu channel. We describe here the seismic signature of a lake-breakout
24 lahar over the course of 85 km along the Whangaehu river system using three 3-component
25 broadband seismometers installed <10 m from the channel at 7.4, 28, and 83 km from the
26 crater lake source. Examination of 3-component seismic amplitudes, frequency content, and
27 directionality combined with video imagery and sediment concentration data were used. The
28 seismic data shows the evolution of the lahar as it transformed from a highly turbulent out-
29 burst flood (high peak frequency throughout), to a fully bulked up multi-phase
30 hyperconcentrated flow (varying frequency patterns depending on the lahar phase) to a slurry
31 flow (bedload dominant). Estimated directionality ratios show the elongation of the lahar with
32 distance down channel, where each recording station shows a similar pattern, but for differing
33 lengths of time. Furthermore, using directionality ratios shows extraordinary promise for lahar
34 monitoring and detection systems where streamflow is present in the channel.

35 **1. Introduction**

36 Volcanic mass flows (e.g. debris flows, pyroclastic density currents, debris avalanches) are one
37 of the greatest threats to communities, industry, recreation, etc. on and around volcanoes.
38 These volcanic mass flows are particularly dangerous as they are fast moving turbulent flows
39 that can occur without any warning or an eruption transpiring (Capra et al., 2010). These flows
40 can move a sizable amount of liquid and debris great distances that can critically impact

41 locations hundreds of kilometers from the volcano or source. Lake-breakout or outburst flood
42 events can be particularly destructive because they tend to be larger and can cause long lasting
43 changes to the landscape and surrounding ecosystems (O'Connor et al., 2013; Procter et al.,
44 2021). Furthermore, unlike eruption or rain triggered mass flows, outburst floods have very
45 little to no warning. Eruption sources can be prepared for by the onset of the eruption and/or
46 the monitoring of the volcano through various methods (e.g. seismology, infrasound, gravity,
47 gas and water chemistry). Likewise, for rain-induced flows using techniques such as the amount
48 or intensity of rain (e.g. Capra et al., 2010; 2018) or by monitoring the amount of available
49 material (e.g. Iguchi, 2019) can help forecast when an event may occur.

50 In New Zealand, there have been numerous cases of large damaging mass flows in modern
51 times. In October 2012, a lake-breakout lahar originating from Te Maari, destroyed hiking trails
52 and forestry, eventually flowing over 4.5 km to damage and block off Highway 46 (Procter et al.,
53 2014; Walsh et al., 2016). Moreover, on 24 December 1953, the deadliest lahar in New Zealand
54 history occurred killing 151 people when a lahar struck a train crossing at the Tangiwai Rail
55 Bridge, 39.8 km from the Crater Lake on top of Mt. Ruapehu (O'Shea, 1954). The ability to
56 predict and investigate the changing dynamics and properties of large volcanic mass flows as
57 they progress down channel is the first step in beginning to understand flow mechanisms
58 better, and ultimately address the hazards involved to mitigate the risk.

59 In order to better characterize and understand these flow events, many applications and
60 instruments have been used in the past (e.g. trip wires, stage gauge, load cells, pore pressure).
61 While many of these tools can yield quick assessments and provide ample warning (e.g. current

62 meters, trip wires), they can sometimes be at risk of false detections, equipment damage or
63 loss, and/or lack the capability to evaluate multiple pulses or flow events. Geophysical
64 instruments (e.g. seismometers, geophones, infrasound) on the other hand can be installed at a
65 safe distance away from the channel and have shown signs of not only being capable warning
66 systems (e.g. Coviello et al., 2019), but have the ability to accurately estimate flow properties
67 (e.g. Arattano and Marchi, 2005; Doyle et al., 2010; Schimmel et al., 2021), as well as flow
68 dynamics (e.g. Gimbert et al., 2014; Coviello et al., 2018; Walsh et al., 2020). However, in order
69 to fully utilize these instruments, improved interpretation, comprehension, assessment, and
70 universality is needed. One technique to increase the ability to predict, warn, and estimate the
71 properties and dynamics of flow events is to use all three components of the seismic recording.
72 Recently, several studies have shown that using all three components is effective in
73 characterizing flow events (e.g. snow-slurry lahars, Cole et al., 2009; snow avalanches, Kogelnig
74 et al., 2011; streamflow, Roth et al., 2016; landslides, Surinach et al., 2005; lahars, Walsh et al.,
75 2020; rockfalls, Kuehnert et al., 2021; hyperconcentrated flows, Walsh et al., 2016). Using the
76 horizontal components along with the vertical component can yield additional information
77 about the flow that is not utilized if only the vertical component is used. Notably, directionality
78 analysis (e.g. Doyle et al., 2010; Walsh et al., 2020) can provide information about wetted
79 perimeter, sediment concentration, and number of particle collisions. Furthermore, differing
80 energies and frequency outputs from channel parallel and channel perpendicular signals can
81 point to specific changes within the flow (Burtin et al., 2010; Roth et al., 2016) that can provide
82 insights into the internal dynamics.

83 **1.1 Anatomy of lahars**

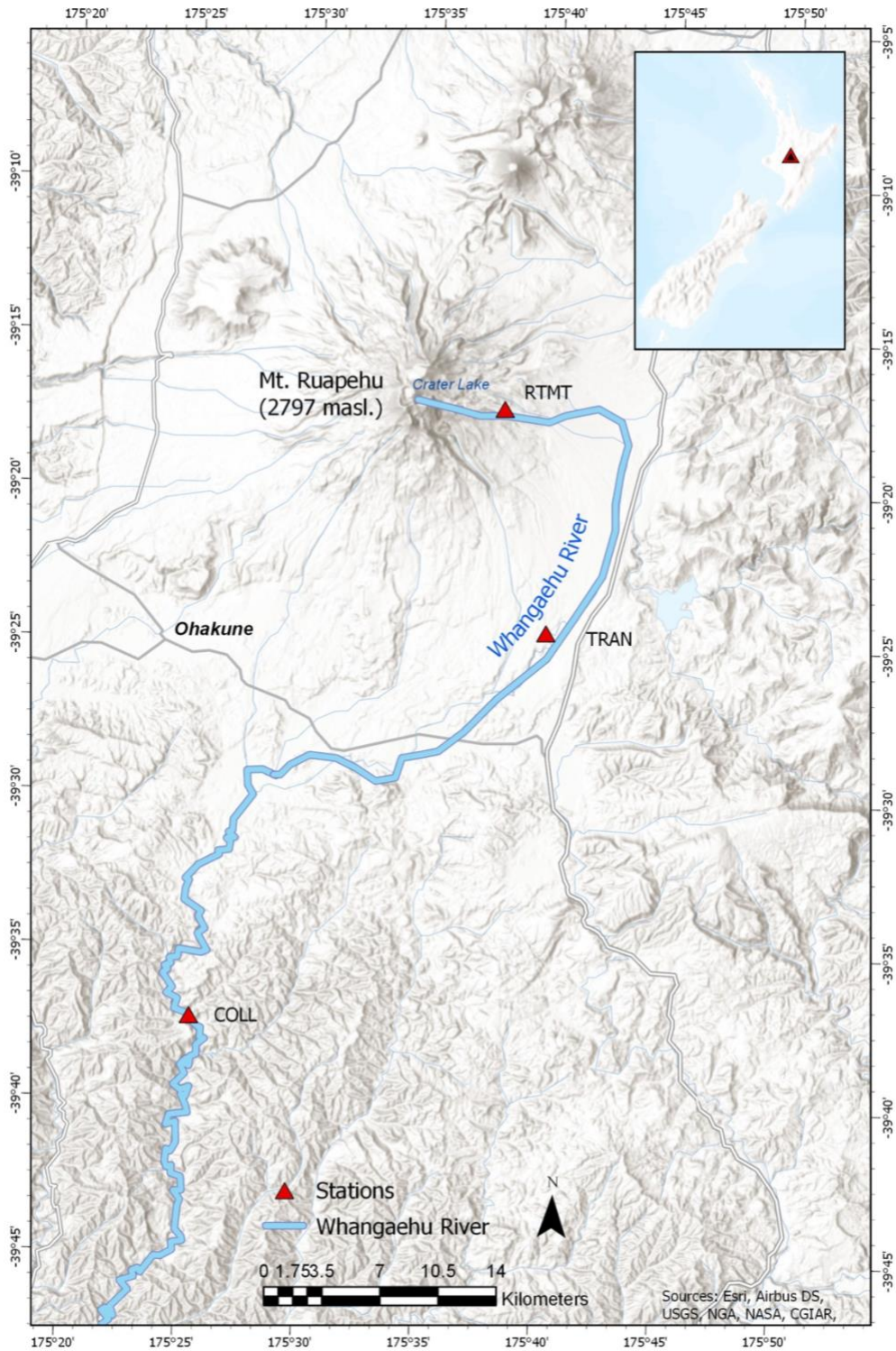
84 When a lahar is created from a lake-breakout or outburst flood event, the transition from flood
85 or streamflow torrent depends on the erosivity of the channel and the supply of sediment being
86 entrapped within the flow (e.g. Scott, 1988; Doyle et al., 2011). An event may start as a highly
87 turbulent low sediment flow, then transform into a hyperconcentrated flow, and may even
88 eventually 'bulk up' to exhibit characteristics of a debris flow with the possibility of laminar or
89 plug-like behavior (Scott, 1988, Pierson et al., 1990). At Mt. Ruapehu, the propagational
90 differences of lahars down channel have been observed and characterized in the past (e.g.
91 Cronin et al., 1996; Cronin et al., 1999; Cronin et al., 2000; Manville et al., 2000; Procter et al.,
92 2010a; Lube et al., 2012). From these studies, models of how lahars bulk up and transition
93 throughout the run-out distance have been postulated. For the lahars in the Whangaehu
94 channel, Cronin et al. (1999) created three 4-phase conceptual models based on source
95 distances of 23.5 km, 42 km, and >55 km. The first two models are for lahar regimes, whereas
96 the third model described a lahar almost at its peak run-out distance. In each model, the first
97 phase consists of a super charged streamflow pulse that flows ahead of the head of the flow.
98 This phenomenon has also been noted for debris flows interacting with streamflow (Arattano
99 and Moia, 1999). Furthermore, discharge is maximum at the transition between phase 1 and
100 phase 2 (Cronin et al., 1999). Phase 2 is described as a mixing zone between streamflow and
101 increasing sediment content, where the peak sediment concentration usually occurs at the end
102 of phase 2 or at the beginning of phase 3 (e.g. Pierson and Scott, 1985). Cronin et al. (1999)
103 defined phase 3 as the lahar body, which has the least amount of the original streamflow
104 contained within. Phase 3 is also characterized by coarse sediment suspensions and is the most
105 likely location for debris flow rheology. Finally, phase 4 is the tail of the lahar where debulking

106 and dilution occurs transforming the lahar back into a hyperconcentrated, mixed, or
107 streamflow.

108 **1.2 18 March 2007 lake-breakout event**

109 Mt. Ruapehu (2797 asl) is the largest stratovolcano in the central North Island of New Zealand
110 (Figure 1) which sits at the southwestern end of the Taupō Volcanic Zone (TVZ). The volcano has
111 a volume of 110 km³ which is composed of several overlapping cone building formations and
112 surrounding ring plain volcanoclastics (Carrivick et al., 2009; Pardo et al., 2012). On top of the
113 volcano, above the currently active vent sits a 1x10⁷ m³ acidic crater lake (Procter et al., 2010a).
114 The Whangaehu channel is the preferred outlet for Crater Lake water and lahars in recent
115 history (Procter et al., 2012; Procter et al., 2021). The Whangaehu channel is on the eastern
116 flank of Mt. Ruapehu where it runs down across the volcanic ring plane where it eventually
117 heads southwest for ~200 km reaching the Tasman Sea.

118 Prior to the events that took place in the morning local time on 18 March 2007, a heavy
119 rainstorm occurred accumulating about 256 mm of water over the 10 hours prior to the dam
120 breach that led to the outburst flood (Massey et al., 2010). The intense rain caused the Crater
121 Lake to rise an extra 6.4 m above the natural lava formation ledge, which started to cause
122 seepage and extra water entering the Whangaehu gorge (Carrivick et al., 2009). At ~11:18 NZT
123 (UTC +12), the tephra dam collapsed causing 1.3x10⁶ m³ of water to flow out of the lake and
124 into the Whangaehu channel (Procter et al., 2010a). The dam was eroded and undercut in
125 multiple stages resulting in a series of retrogressing landslides along with the main debris
126 flow/lahar channel.



127

128 *Figure 1 Map of Mt. Ruapehu and the surrounding area located on the central North Island of New Zealand. Blue*
 129 *outline represents the Whangaehu channel and the path the 18 March 2007 lahar traveled down. Red triangles*
 130 *denotes the three monitoring stations along the Whangaehu channel at 7.4, 28, and 83 km.*

131 Since the lahar was caused by lake-breakout dynamics and thus an abundance of water, the
132 event was classified as a hyperconcentrated streamflow rather than a sediment-filled debris
133 flow (Procter et al., 2010b). At ~8.0 km from source velocity measurements recorded the flow
134 at ~ 9.5 m/s and had an estimated 6 m of downcutting showing the ability for the lahar to
135 deposit and erode massive amounts of material (Procter et al., 2010a,b). Furthermore, the 18
136 March 2007 lahar was one of the most thoroughly monitored lahars ever (Manville and Cronin
137 2007). In total there were 21 monitoring locations setup to measure various lahar properties,
138 (e.g. flow monitor, camera, stage height, flow sampling, pore-pressure, seismic, etc.) along the
139 channel (Keys and Green, 2008; Lube et al., 2012), with the lahar taking over 16 hours to
140 eventually travel out to the New Zealand coast, ~200 km from the original crater lake source.

141 Here, we delve into the properties of a lake-breakout hyperconcentrated streamflow that
142 bulked up to a volume of $\sim 4.4 \times 10^6 \text{ m}^3$ (Procter et al., 2010a) over the course of 83 km that
143 occurred on 18 March 2007 along the Whangaehu channel originating from Mt. Ruapehu, New
144 Zealand. The combination of seismic analysis (frequency and directionality) with supplementary
145 measurements (e.g. video, sediment concentration) show how a lahar transforms over time and
146 distance and how using these seismic techniques can help monitor the ever changing dynamics
147 and properties of a flow event. Furthermore, we examine previous models of the evolution of a
148 lahar and compare the model with the seismic data available.

149 **2. Data**

150 The seismic data for the 18 March 2007 lahar was recorded on three seismometers installed at
151 various distances (7.4, 28, 83 km) along the Whangaehu channel (Figure 1). The three 3-

152 component broadband Guralp 6T sensors (COLL, RTMT, TRAN) recorded data at 100 Hz
153 sampling and had GPS time stamps. For each site, the seismometers axes were installed to true
154 North and the recorded data were rotated to align North as flow parallel (P) and East as the
155 cross-channel direction (T). Furthermore, the seismometers were installed normal to horizontal
156 to lessen the degree of vertical energy transfer to the horizontal components. The monitoring
157 station Round the Mountain Track (RTMT), was installed 4 m from the channel and 7.4 km
158 downstream from the source of the lahar. The lahar arrived at RTMT at 23:36 UTC and had an
159 average velocity of 9.3 m/s (Figure 2a). The Trans Rail Gauge (TRAN) station was installed 28 km
160 from source and 10 m from the channel, which also included a video camera that captured an
161 image every 30 seconds. The lahar arrived at TRAN at 24:35 UTC with an average velocity of 5.6
162 m/s (Figure 2d). The Colliers Bridge (COLL) station was installed 10 m from the channel and 83
163 km from source. The lahar arrived at COLL at 04:13 UTC and had an average velocity of 4.8 m/s
164 (Figure 2f). Arrival times are based off of images and eye witnesses at each of the monitoring
165 stations. The flow velocity at RTMT and COLL were estimated from imagery and at TRAN from a
166 flow meter.

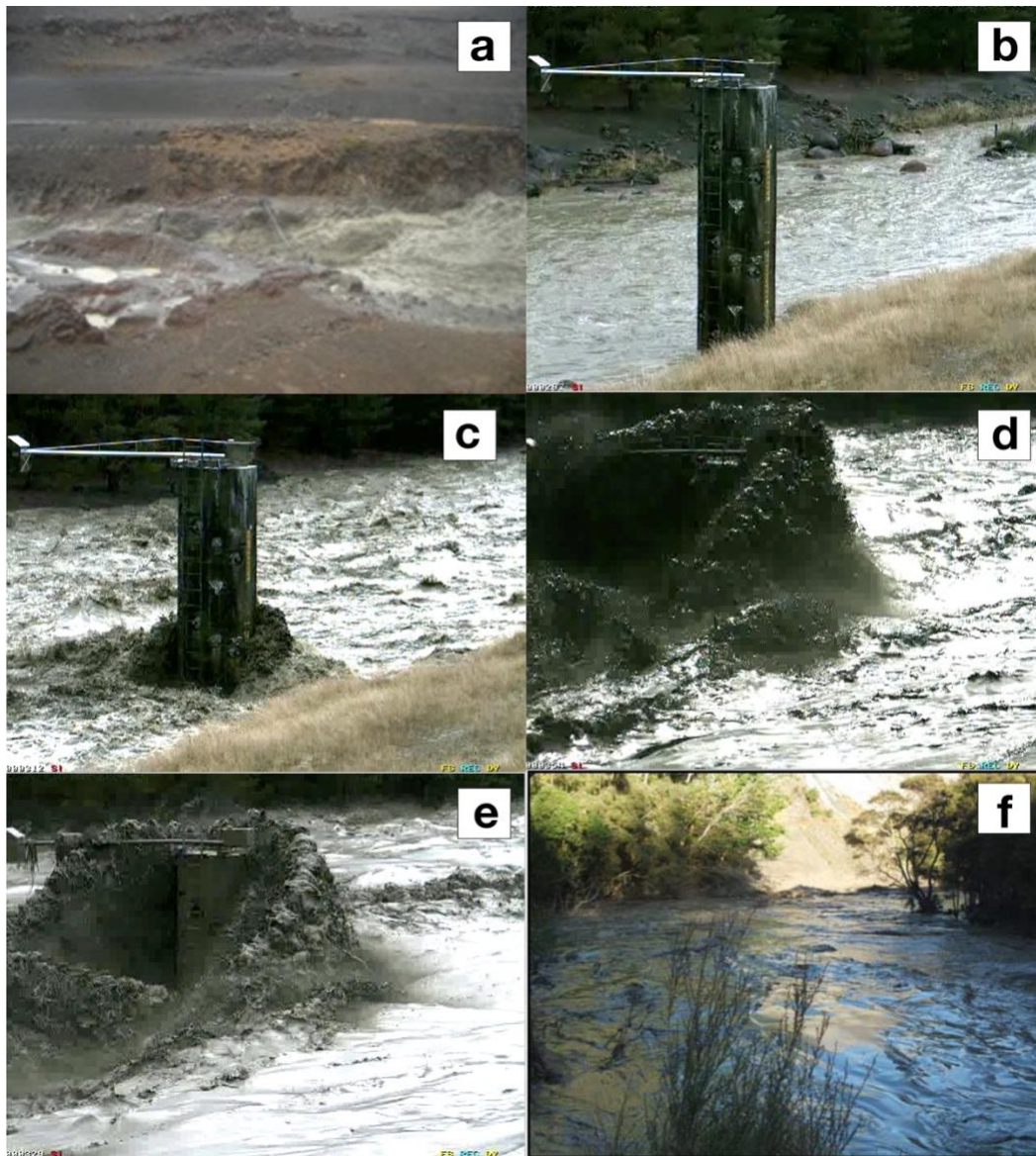
167 **3. Results**

168 To examine the multi-component dynamics of the 18 March lake-breakout event along the
169 Whangaehu channel at three monitoring locations, the data were corrected for instrument
170 response and split into 10 s time windows. At each recording location, peak spectral frequency
171 (PSF) amplitude, root mean squared (RMS) amplitude, and directionality ratios (DR) are
172 estimated for each of the 10 s time windows. At each monitoring station the first hour of the

173 lahar including five minutes prior to the arrival are shown in all the results except when
174 indicated.

175

176

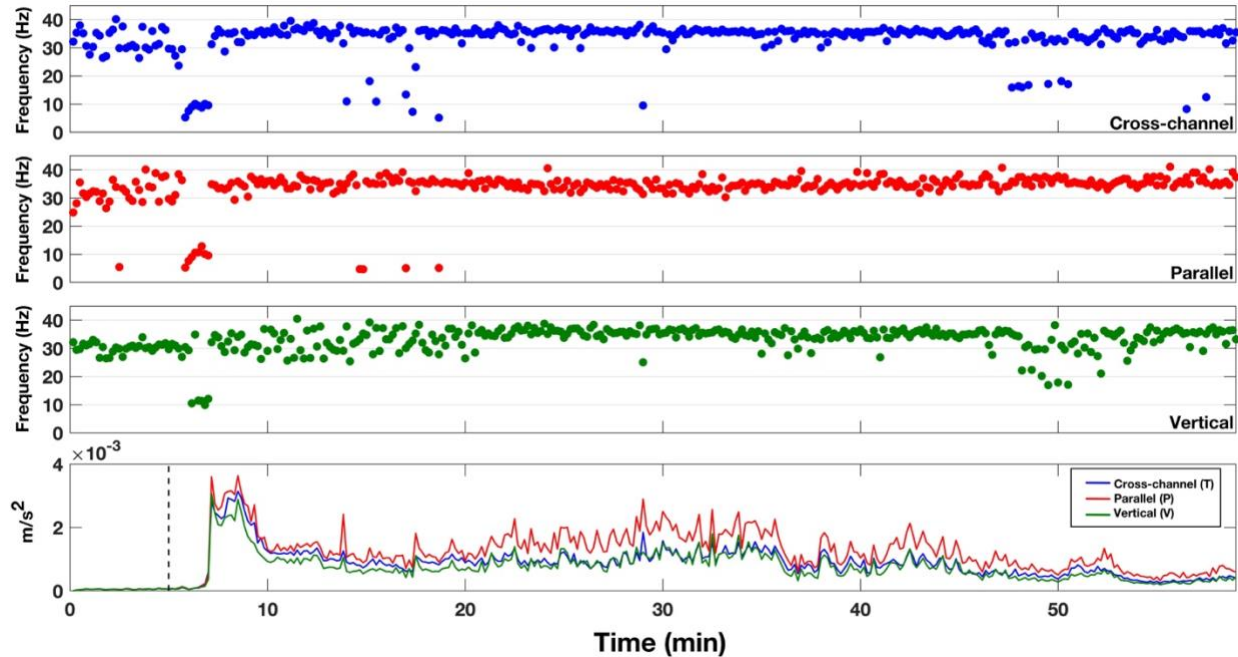


177

178 *Figure 2 Images from the 18 March 2007 lake break-out lahar from RTMT (a), TRAN (b, c, d, e), and COLL (f). Note*
179 *the transformation of the lahar at TRAN from streamflow (b), increased discharge pre-lahar phase 1 pulse (bow*
180 *wave) (c), head of the lahar (d), and low PSF beginning of lahar body (e).*

181 **3.1 Frequency analysis**

182 In order to examine the PSFs for all three components at each site along the channel, we use
183 the frequency recorded at the maximum amplitude of the frequency spectra for each 10 s
184 running time window. The PSF for RTMT (7.4 km from source) shows similar patterns between
185 all three components (Figure 3). The five minutes prior to the arrival of the head (peak seismic
186 amplitude) of the lahar are characterized by scattered PSFs between 20-40 Hz for the cross-
187 channel (Figure 3, blue dots) and parallel (Figure 2, red dots) directions, while in the vertical
188 direction (Figure 3, green dots) the PSF is ~ 30 Hz. When the front of the lahar arrives at the
189 station, the PSF in all three components decreases to ~ 5 -10 Hz for about 1 min before
190 increasing again to higher frequencies. After the front of the lahar passes the station and when
191 the head arrives the PSF in the cross-channel and parallel directions remain between 30-40 Hz
192 for the rest of the recording window. In the vertical component, the PSF is scattered between
193 20-40 Hz for ~ 15 min after the arrival of the head of the lahar and then becomes narrower,
194 similar to both the cross-channel and parallel components with PSFs between 30-40 Hz.



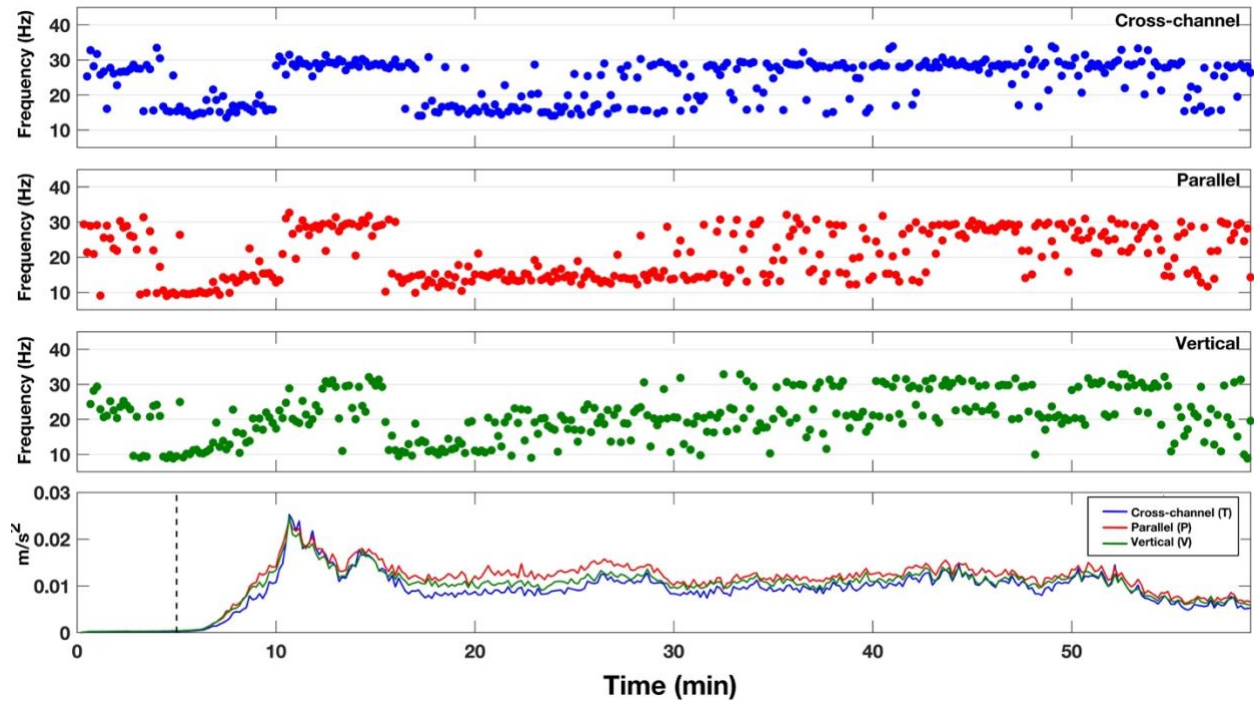
195

196 *Figure 3 Peak spectral frequencies for RTMT (7.4 km from source) for cross-channel (blue dots), flow parallel (red*
 197 *dots), and vertical (green dots) directions. Bottom row depicts the RMS amplitude of the lahar color coded to the*
 198 *same colors as the PSF. The dashed vertical line marks the timing of the lahar front passing the monitoring station.*
 199 *All PSFs and RMS amplitudes were calculated using 10 s time windows.*

200 Further down the channel at station TRAN (28 km from source), the PSFs for all three
 201 components show a similar overall pattern (Figure 4). The pre-lahar PSF distribution in all three
 202 components is between 20-32 Hz. Like RTMT higher up the channel, the PSFs for the front of
 203 the lahar at TRAN first drops down to around 10 Hz and when the lahar head arrives (10 min,
 204 Figure 4) the PSF increases to ~30 Hz for parallel (Figure 4, red dots) and cross-channel (Figure
 205 4, blue dots) directions and between 20-30 Hz in the vertical component. This decrease to
 206 lower frequencies before the head of the lahar at TRAN lasts for about 5 min. After the head of
 207 the lahar passes the recording station the PSF content decreases for ~15 min to 10-20 Hz for
 208 the parallel and cross-channel components and between 10-25 Hz for the vertical (Figure 4,
 209 green dots) components. The PSF after the 30 minute mark in Figure 4 displays a bimodal

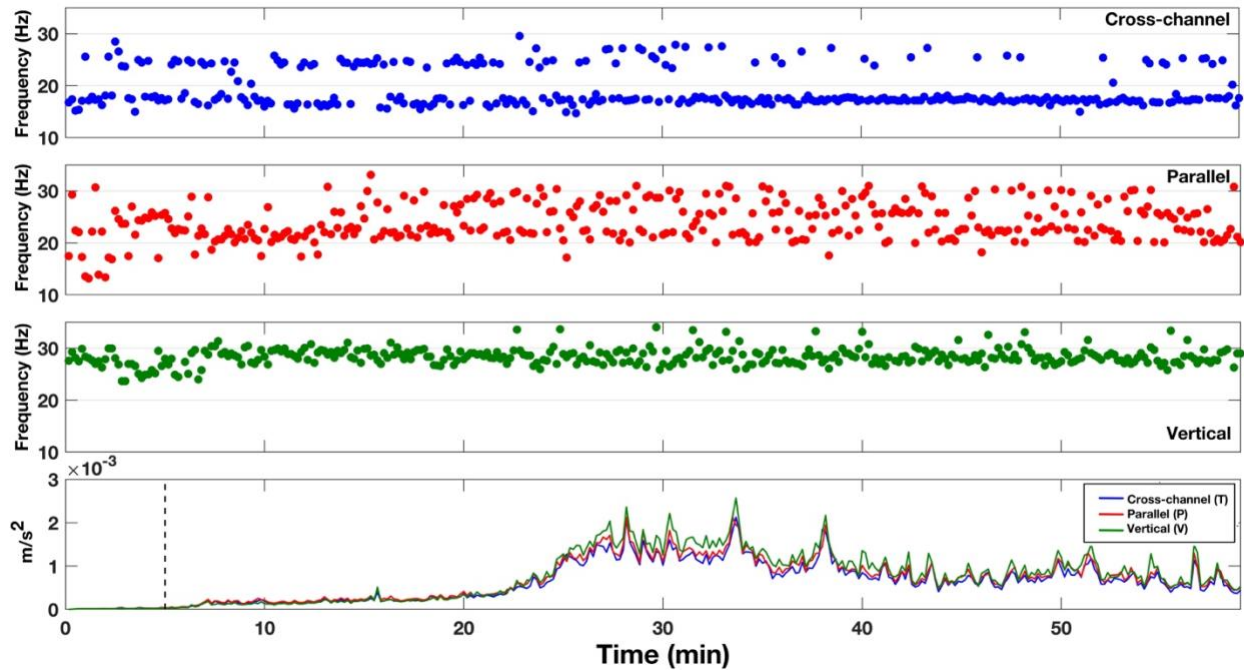
210 pattern with frequencies between 10-35 Hz, with PSF time windows concentrating most at ~30
211 Hz.

212 At the COLL recording station (83 km from source), the PSF distribution shows differing patterns
213 for all three components (Figure 5). The PSF in the cross-channel direction (Figure 5, blue dots)
214 depicts a bimodal pattern throughout with a strong lower concentration of time windows at
215 ~18 Hz and a higher PSF at ~25 Hz. For the parallel component (Figure 5, red dots), the pre-
216 lahar signal has a wide PSF range between 12-30 Hz. When the lahar arrives, the PSF becomes
217 concentrated at ~22 Hz for ~8 min before transforming into a bimodal pattern similar to that of
218 the cross-channel PSF, with frequencies between 20-30 Hz. In the vertical component (Figure 5,
219 green dots), the PSF remains concentrated around ~28 Hz, only varying just prior to the arrival
220 of the lahar and during the highest energy stage of the lahar (25-40 min).



221

222 *Figure 4 Peak spectral frequencies for TRAN (28 km from source) for cross-channel (blue dots), flow parallel (red*
 223 *dots), and vertical (green dots) directions. Bottom row depicts the RMS amplitude of the lahar color coded to the*
 224 *same colors as the PSF. The dashed vertical line marks the timing of the lahar front passing the monitoring station.*
 225 *All PSFs and RMS amplitudes were calculated using 10 s time windows.*



226

227 *Figure 5 Peak spectral frequencies for COLL (83 km from source) for cross-channel (blue dots), flow parallel (red*
 228 *dots), and vertical (green dots) directions. Bottom row depicts the RMS amplitude of the lahar color coded to the*
 229 *same colors as the PSF. The dashed vertical line marks the timing of the lahar front passing the monitoring station.*
 230 *All PSFs and RMS amplitudes were calculated using 10 s time windows.*

231 3.2 Directionality

232 When recording mass flows with 3-component sensors, the directionality may be examined due
 233 to the sensor being able to record signals in the two horizontal directions. The directionality
 234 ratio allows for the determination of which horizontal component has stronger energy over the
 235 course of the recording window. This is possible because, in channel side deployments for mass
 236 flow monitoring systems, the sensor is either installed so that the North component is aligned
 237 to be parallel to the flow or can be rotated during the data processing stage to align with the
 238 channel orientation. Furthermore, with the channel side installations, attenuational factors can
 239 mostly be ignored due to the close proximity to the channel and energy output of the flow
 240 event. The directionality ratio (DR) can be defined as the cross-channel amplitude divided by

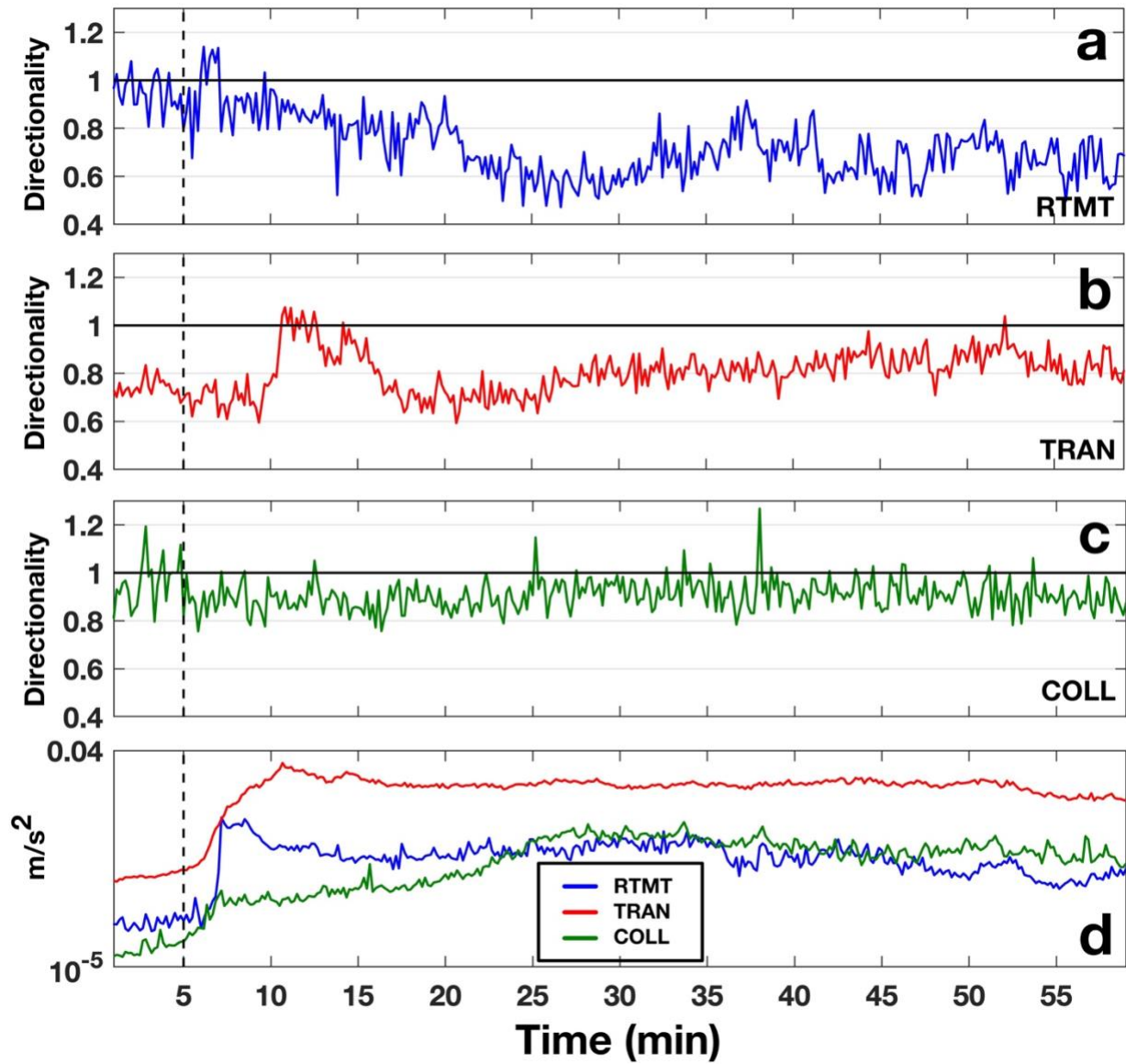
241 the flow parallel amplitude. A DR > 1 indicates that the cross-channel amplitude is larger than
242 that of the flow parallel, and vice-versa for a DR < 1. Directionality ratios have been used in the
243 past to show rheology changes within flows for warning purposes, where the DR increases
244 when streamflow transitions into a lahar (Walsh et al., 2020), and have been hypothesized to
245 be an indicator for flow properties such as sediment concentration, wetted perimeter, and/or
246 amount of particle collisions within a lahar (Doyle et al., 2010).

247 The directionality ratios for 10 s running time windows at each seismic station for the 18 March
248 2007 lake-breakout lahar are shown in Figure 6. The DR for RTMT (Figure 6a) displays a DR
249 around 1 pre-lahar, then decreases right before the lahar arrives at the recording station
250 (Figure 6, dashed line), then as soon as the lahar passes, the DR increases to above DR = 1 for
251 ~2 min. After the initial lahar flood pulse passes RTMT, the DR then proceeds to decrease below
252 a DR = 1 for the rest of the recording window. Similar to RTMT, the DR for TRAN starts out with
253 a DR < 1 (0.7-0.8) and as the lahar front passes, the DR similarly decreases to 0.6-0.7 before
254 increasing to a DR > 1 for ~5 min when the lahar is at peak energy output starting at about the
255 10 min mark (Figure 6d, red line). After the passing of the peak energy, the DR for TRAN
256 decreases below 1 again for the remainder of the recording window. Further down the channel
257 at COLL (Figure 6c), the DR before the lahar arrives has a wide range of values between 0.8-1.2.
258 When the front of the lahar passes (Figure 6, dashed line), the DR stabilizes between 0.8-1,
259 before increasing slightly when the peak energy of the lahar passes the monitoring site at about
260 the 25 min mark.

261

262

263



264

265 *Figure 6 Directionality ratio plots over time for RTMT (a), TRAN (b), and COLL (c). Vertical RMS seismic signals for*
266 *the three stations are plotted in (d) where blue is RTMT, red is TRAN and green represents COLL. The dashed*
267 *vertical lines mark the timing of the lahar front passing the monitoring station. All DRs and RMS amplitudes were*
268 *calculated using 10 s time windows.*

269 **4. Discussion**

270 4.1 Frequency constraints

271 In order to obtain an understanding if PSFs are able to properly describe the lahar dynamics (i.e.
272 the weight of the spectral amplitude at the PSF), frequency constraints must be analyzed. To
273 complete this, normalized spectrograms along with spectral centroidal frequency (SCF) and
274 spectral spreads are computed. The normalized spectrograms are estimated by normalizing the
275 spectral amplitude for each 10 second time window of the lahar individually. By normalizing
276 each time window, ranges of dominant frequencies can be visualized. SCFs are used because
277 they represent the weighted average of the spectra, and yield the location (i.e. frequency) of
278 the center of the spectral mass. The SCF of each time window is estimated similar to that of
279 Saló et al. (2018), in which:

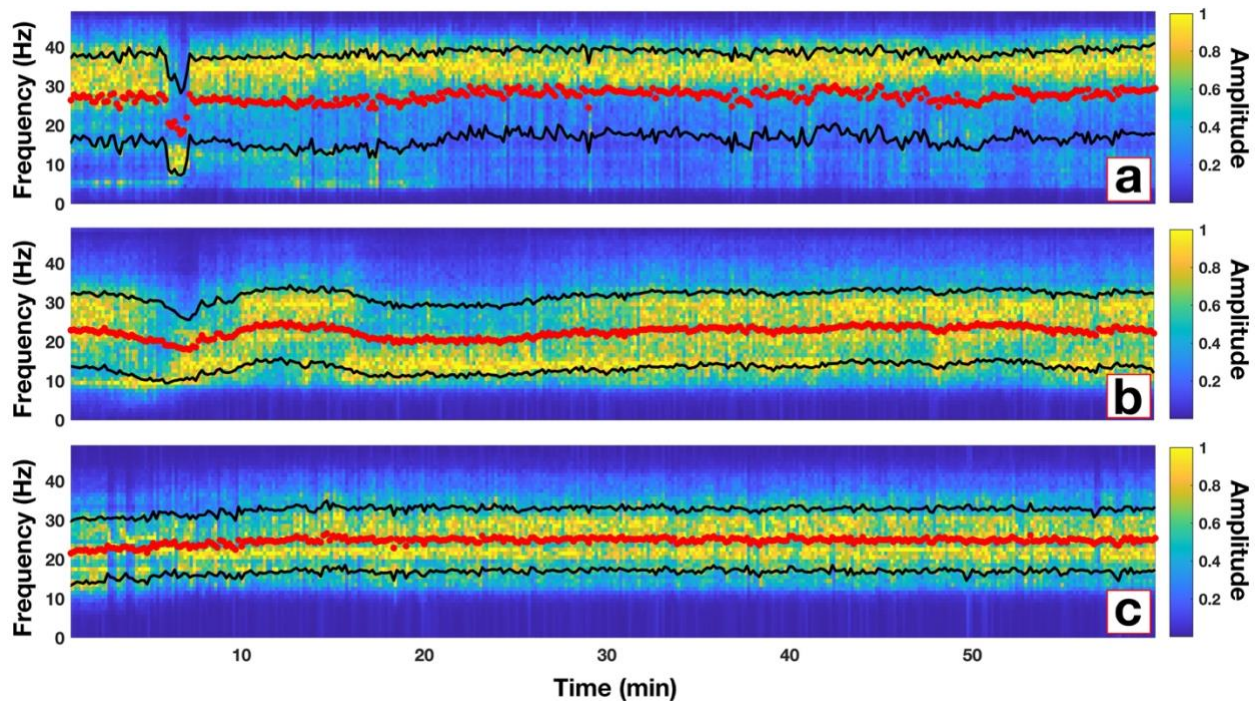
$$280 \quad SCF = \frac{\sum_{f_1}^{f_2} f * A(f)}{\sum_{f_1}^{f_2} A(f)} \quad (1)$$

281 where f is the frequency and $A(f)$ is the spectral amplitude associated with each frequency bin.
282 The spectral spread measures the width of the spectral energy around the SCF, thus yielding
283 information about the quality of the PSFs. Spectral spread can be estimated by:

$$284 \quad S = \sqrt{\frac{\sum_{f_1}^{f_2} (f - SCF)^2 * A(f)}{\sum_{f_1}^{f_2} A(f)}} \quad (2)$$

285 The computed normalized spectrograms along with SCFs and spectral spreads for each of the
286 three monitoring stations are shown in Figure 7. For simplicity and comparison, only the flow
287 parallel data are shown. The normalized spectrograms for every station and component can be
288 seen in Figures S1-S3.

289 The normalized spectrogram for RTMT (Figure 7a) yields very similar results to that of the PSF
290 (Figure 3b), where most of the higher spectral amplitudes are at the same frequencies as those
291 of the PSF. Notably, the low ~ 10 Hz signal immediately before the arrival of the head of the
292 lahar is not only seen in the dominate normalized spectra, but also through the decrease in SCF.
293 Additionally, the PSFs at these time windows are contained within the spectral spread (Figure
294 7a, black lines). For TRAN, the normalized spectrogram (Figure 7b) is again, very similar to the
295 PSF in Figure 4b. The SCF mirrors the pattern of the PSF with higher frequencies for the
296 streamflow, a decrease for the front of the lahar, increase for the head of the lahar, decrease
297 after the passing of the head, and finally a slight increase later in the lahar body. The
298 normalized spectra yields this same pattern, with the late lahar body displaying the only
299 timeframe with increased spectral amplitude distributed throughout the spectral spread (Figure
300 7b, after 30 min). This most likely explains the bimodal distribution of PSFs for TRAN in Figure 4
301 after the ~ 30 min mark. Continuing, the normalized spectrogram for COLL (Figure 7c), also
302 shows similarities to that of the PSFs in Figure 5b. The PSFs for COLL range between ~ 20 -30 Hz
303 with a slight bimodal pattern. This same pattern can be seen where the higher spectral
304 amplitudes are located (Figure 7c). Furthermore, the SCF for COLL splits the PSF range and stays
305 at ~ 25 Hz during the bimodal phase of the PSF. Overall, with the analysis of the normalized
306 spectrograms, SCFs and spectral spreads, we confirm that the use of PSFs to describe mass flow
307 dynamics is concise for the 18 March 2007 lake-breakout lahar.



308

309 *Figure 7 Normalized spectrograms for the flow parallel direction for each of the three monitoring sites along the*
 310 *Whangaehu channel. Red dots represent the spectral centroidal frequency and black lines show the range of the*
 311 *spectral spread. Note, normalized spectrograms for the other directions can be seen in Figures S1-S3.*

312 **4.2 Evolution of lahar signals**

313 A lahar propagating down channel can bulk up by collecting material from erosion or through
 314 the coalescing of multiple pulses to shorten the total length of the lahar (Procter et al., 2010;
 315 Doyle et al., 2011). Lahars can also debulk by depositional means or by the natural elongation
 316 of the lahar as it progresses down channel (Doyle et al., 2011; Lube et al., 2012). Considering
 317 the 18 March 2007 lake-breakout lahar was a large pulse of water that only mixed with the
 318 existing streamflow and contained no juvenile material, examining the seismic signatures along
 319 the flow path can be used to characterize the evolution and transformation of a lake-breakout
 320 event from outburst flood to hyperconcentrated flow and beyond. At RTMT (Figure 3), the
 321 seismic signature is dominated by the flow parallel direction with > 30 Hz PSF. The exception to

322 this is the timeframe immediately before the head of the lahar passes when the PSF decreases
323 to ~10 Hz. This low frequency signal can be seen at TRAN (Figure 4) and in the flow parallel
324 component at COLL (Figure 5, red dots). However, at COLL the PSF is ~20 Hz instead of 10 Hz as
325 in RTMT and TRAN due to flow properties at 83 km from source. This low PSF before the head
326 of the lahar arrives at the station could represent the supercharged stream flow pulse (bow
327 wave) that is pushed in front of the head of the lahar as described by Cronin et al. (1999) where
328 they noticed these same pulses in front of lahar heads for three lahars on Mt. Ruapehu in 1995.
329 Conversely, this frontal pulse could be from the uplift of streamflow from the faster moving
330 underflow of the lahar (Manville et al., 2000). Furthermore, the low frequency zone before the
331 head of the flow lengthens as the lahar progresses downstream, suggesting that lahar
332 elongation can also be seen in the seismic frequency domain. The ~10 Hz PSF may be explained
333 by flow processes (Schmandt et al., 2013; Barriere et al., 2015; Bartholomaeus et al., 2015) and
334 could be due to the flow at this stage being more sensitive to discharge (Gimbert et al., 2014;
335 Schmandt et al., 2017; Anthony, et al., 2018) or in the case of the underflow hypothesis,
336 frictional sliding on the channel bed (Huang et al., 2004). The frontal surge or phase 1 of the
337 lahar can be seen in the DR (Figure 6) as well. For every station along the channel the DR has a
338 slight drop when phase 1 passes the recording station (Figure 6, dashed line). The elongation of
339 phase 1 can also be seen, where the dip in the DR is only ~1 min for RTMT, ~5 min for TRAN,
340 and approximately 20 min for COLL. The reason the DR decreases during phase 1 for the 2007
341 lahar could be due to the parallel component being more sensitive to flow processes than
342 bedload forces (Barriere et al., 2015; Roth et al., 2016). During phase 1 discharge increases,
343 sediment concentration is low, and streamflow dominates resulting in a low DR (e.g. Doyle et

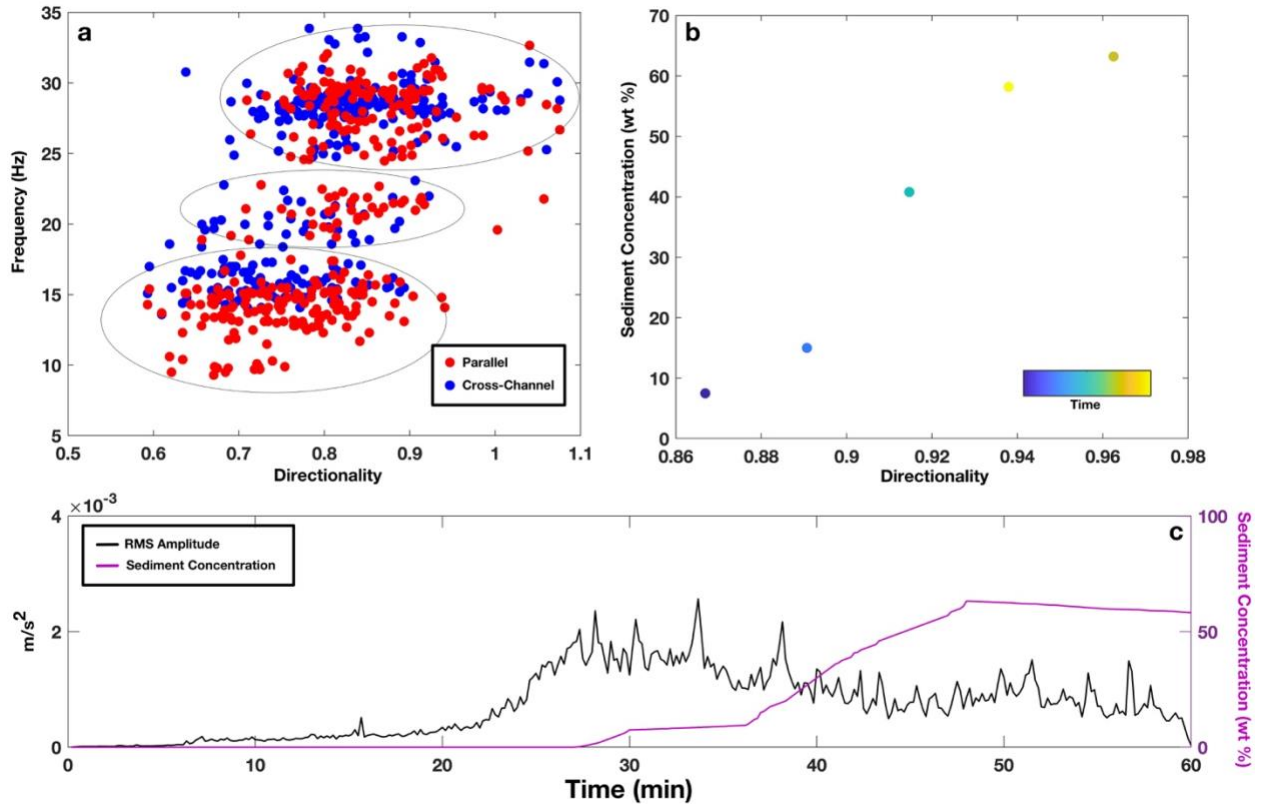
344 al., 2010). The low DR can also be seen before the arrival of phase 1, due to streamflow already
345 occurring in the channel. The higher flow parallel amplitude over cross-channel amplitude for
346 streamflow has also been noted in the past for lahars at Volcán de Colima, Mexico (Walsh et al.,
347 2020).

348 Following the low PSF phase 1 (i.e. front of the lahar), the peak seismic amplitude occurs. The
349 peak seismic amplitude for RTMT is accompanied by an increase to higher PSFs > 30 Hz (Figure
350 3, 7a). PSFs > 30 Hz have been shown in the past to be either dominated by turbulence or
351 bedload transport (e.g. Gimbert et al., 2014; Roth et al., 2016). The 2007 lake-breakout lahar
352 has been described as a hyperconcentrated streamflow (e.g. Procter et al., 2010b) with low
353 sediment concentration, especially early on before the lake water captured enough material to
354 bulk up into a full 4-phase lahar (see section 1.1). At RTMT, which was only 7.4 km from source,
355 the lahar had not fully bulked up yet and was in a net depositional regime (Procter et al.,
356 2010a). Due to the conditions of the lahar at RTMT, we surmise the higher PSF content for the
357 peak seismic amplitude is dominated by turbulent-flow-induced noise. Furthermore, the higher
358 PSF content at RTMT compared to TRAN and COLL (~30 Hz) could be due to the angle of the
359 slope at the recording stations. Gimbert et al. (2014) noted that turbulence noise will dominate
360 over bedload-induced noise on steeper slopes. Further down the channel at TRAN, the PSF for
361 the peak seismic amplitude is ~30 Hz for all three components. Again, this high PSF can be
362 attributed to turbulence as seen by the images taken at TRAN (Figure 2d). The difference at
363 TRAN is the length of the higher PSF, where at RTMT the high PSF stays throughout the entirety
364 of the recording window, at TRAN the high PSF and seismic amplitude only last for ~5 min. The
365 difference at TRAN could be from the evolution of the lahar. By time the lahar reached the

366 monitoring station at TRAN (28 km from source) the lahar was fully bulked up and had the
367 properties of a traditional four phase lahar as described by Scott (1988) or Cronin et al. (1999).
368 By time the lahar reached COLL 82 km from source, the peak seismic amplitude is associated
369 with PSFs between 15-30 Hz, with bimodal patterns in the horizontal components and a tighter
370 spread in the vertical component (~27-29 Hz). At COLL, the lahar had converted into a plug-like
371 flow with lower turbulence and hence the higher PSFs are most likely associated with bedload
372 transport (Figure 2f). Furthermore, Burtin et al. (2010) and Roth et al. (2016) noted that when
373 the vertical component has greater seismic amplitudes than the horizontal components,
374 bedload dominates. This same amplitude feature can be seen at COLL (Figure 5, bottom panel)
375 where the vertical energy is greater than each of the horizontal components. The bimodal
376 pattern of the horizontal components is likely to be the recording of both turbulence or flow
377 properties (lower PSF) and bedload transport (higher PSF). This also explains why the vertical
378 component does not show the same bimodal pattern. Barriere et al. (2015) described the
379 parallel component as being more sensitive to flow properties, and Doyle et al. (2010) noted
380 that the cross-channel component is likely dominated by turbulence, thus the reasoning behind
381 the differing PSF patterns between components. This PSF feature is similar to the lahars
382 recorded by Walsh et al. (2020), where the cross-channel PSF is confined within a narrow band
383 around 15-20 Hz and the flow parallel PSF is more bimodal. At COLL, the cross-channel PSF is
384 dominated by PSFs at ~18 Hz (lower than vertical component at ~28 Hz), with the flow parallel
385 between 20-30 Hz.

386 The DR at the peak seismic amplitude for all three recording stations increases (Figure 6). The
387 DR for both RTMT and TRAN increases to $DR > 1$. Doyle et al. (2010) noted that higher wetted

388 perimeters will increase the DR, which is true for the 18 March 2007 lake-breakout lahar (Figure
389 6, peak DR/RMS amplitude). Conversely, the DR decreases after the peak seismic amplitude
390 while the wetted perimeter is still high. Also, at COLL the DR only increases slightly with the
391 seismic amplitude. While the wetted perimeter may be a factor in increasing cross-channel
392 energy and thus the DR, the more likely explanation for the 18 March 2007 lahar might be the
393 higher level of particle collisions at the peak seismic amplitude. More particle collisions would
394 increase the DR (e.g. Doyle et al., 2010) due to more lateral excitation within the flow and
395 against the channel walls. The increase in collisional energy also relates well with the PSF, as
396 higher PSF correlates to an increase in the amount of interflow collisions as shown by Huang et
397 al. (2004) and may also explain why DRs correlate well with PSF (Figure 8a). The DR for COLL
398 during this same timeframe probably is not due to the amount of particle collisions due to the
399 plug-like flow (Figure 2f), but rather the increase in sediment concentration (Figure 8c). As the
400 sediment concentration increases at COLL the DR starts to increase as well (Figure 8b). Similar
401 to Doyle et al. (2010), COLL yields a correlation between DR and sediment concentration (Figure
402 8b), where higher DRs indicate higher concentrations of sediment contained in the flow. Lastly,
403 as noted above, DRs may correlate with PSF or at least indicate differing processes taking place
404 within the flow (Figure 8a). Lower PSF would produce lower DRs because low PSF are more
405 sensitive to flow processes (hence higher parallel energy) whereas higher PSFs would produce
406 higher DRs due to higher PSF being dominated by collisions and turbulence (higher cross-
407 channel energy) (Figure 8a).



408

409 *Figure 8 Plots of (a) correlation between PSF and DR at TRAN, (b) sediment concentration and DR at COLL, and (c)*
 410 *seismic amplitude (black line) with sediment concentration (purple line) depicting the lag in sediment at COLL. Note*
 411 *on (a) parallel (red dots) and cross-channel (blue dots) PSF display three different zones (black circles). Also note*
 412 *that at COLL the first sediment concentration measurement did not occur until the 30 min mark.*

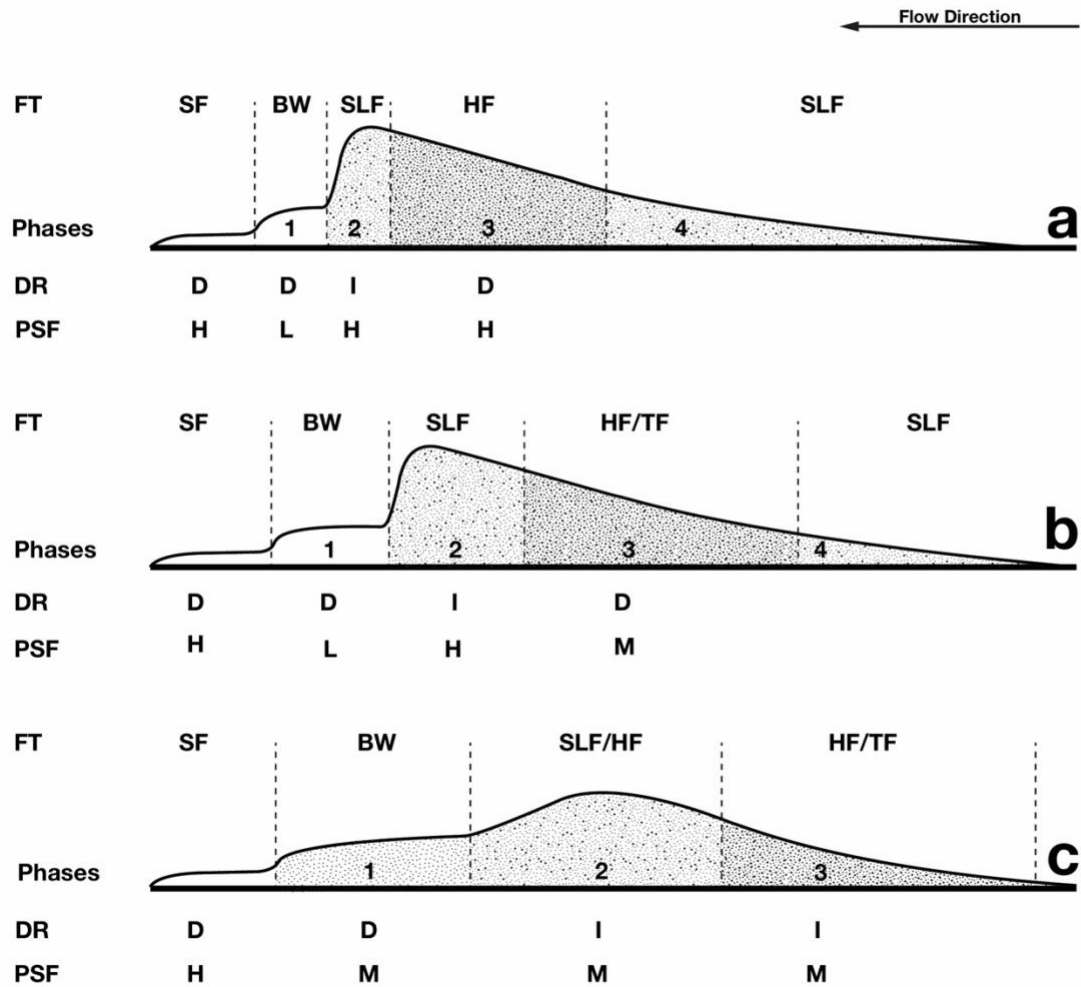
413 While the lahar at RTMT was a large outburst flood/sediment-laden flow, and at COLL a plug-
 414 like flow, at TRAN the 18 March 2007 lahar was a dynamic bulked up “traditional” lahar. The
 415 evidence for this is in the PSF content for TRAN (Figure 4) compared to the other two
 416 monitoring sites. At TRAN the PSF has a step-up step-down pattern for the first 30 min of the
 417 lahar passing, and then transitions to a bimodal or wide PSF range for the rest of the recording
 418 window. As noted above, the low PSF preceding the lahar head arrival is thought to be due to a
 419 sensitivity to water transport properties (Figure 2c). The increase to higher PSFs during the peak
 420 seismic amplitude may be from particle collisions and/or higher turbulence (Figure 2d). After
 421 the maximum seismic amplitude at TRAN, the PSF decreases to 10-20 Hz. This drop in PSF after

422 the highest stage and amplitude could be from a more water transport dominated regime,
423 which can be seen in the increased parallel amplitude (Figure 4, 8a). The decrease may also be
424 from greater frictional sliding on the channel bed (Huang et al., 2004). Furthermore, this PSF
425 range could simply indicate a decrease in turbulence (Figure 2e). After the decrease to 10-20 Hz
426 PSFs, the PSF displays a bimodal or wide frequency range at ~28 min (Figure 4, 7b). As
427 aforementioned for COLL, this PSF pattern could be from both bedload- and water-transport-
428 induced noise. This timeframe is also where the peak sediment concentration would be, as
429 noted by Cronin et al. (1999), and thus the PSF would show more bedload high PSF. This
430 hypothesis also compares well with the DR (Figure 6b), where the cross-channel energy
431 increases starting at ~25 min indicating that the sediment concentration may be increasing
432 (Doyle et al., 2010). Finally, the wide PSF range later in the recording window (Figure 4) could
433 also result from the lahar having two distinct layers as described by Cronin et al. (2000), where
434 there is a wide more dilute finer grain top layer and a channelized sediment-rich layer on the
435 bottom. The two layer model can apply to TRAN because the lahar at this monitoring station
436 overtook the channel (Figure 2d,e) and proceeded to flow horizontally outward forming the
437 surface layer described by Cronin et al. (2000).

438 **4.3 Implications for monitoring**

439 The main goal of this research is to contribute in defining better monitoring criteria for
440 dangerous mass flow events. The data described above is part of a larger collection of
441 monitoring data collected over the entire length of the Whangaehu channel consisting of 21
442 monitoring sites and years of preparation (e.g. Manville and Cronin, 2007; Keys and Green,

443 2008). Due to this, the ability to accurately estimate the properties of the lahar at various
444 stages along its path is possible. When it comes to flow events of any size, the ability to
445 understand how the dynamics change with distance along the channel is important for warning
446 and future hazard mitigation. We show here that a lake-breakout event can start out as an
447 outburst flood, bulk up into a hyperconcentrated flow, then eventually elongate and entrap
448 enough sediment to transform into a plug-like slurry flow. Each of these flow types yields
449 differing PSF ranges and patterns due to the relationship between the channel geometry,
450 sediment concentration, turbulence, and bedload transport. While the lahar at different
451 stations along the channel may have differing PSF content, we also show that the lahar
452 elongates and a predictable model (e.g. Cronin et al., 1999) can be used with and shown in the
453 seismic data. Being able to apply such a model may yield some relevance of universality in
454 terms of warning systems at different distances away from the mass flow source. Whereas
455 shown above, the flow phases at each monitoring station can be seen, but at differing lengths
456 and times in the seismic signal (e.g. Figure 6). To better visualize this concept, conceptual
457 models based off of the Cronin et al., 1999 models are created for each of the three seismic
458 stations for the 18 March 2007 lahar (Figure 9). In the conceptual models for the 2007 lahar,
459 the aforementioned elongation of the frontal pulse or bow wave (phase 1) and head of the
460 lahar (phase 2) is shown, along with the differences and similarities between the properties of
461 the lahar at the three seismic monitoring sites.



462

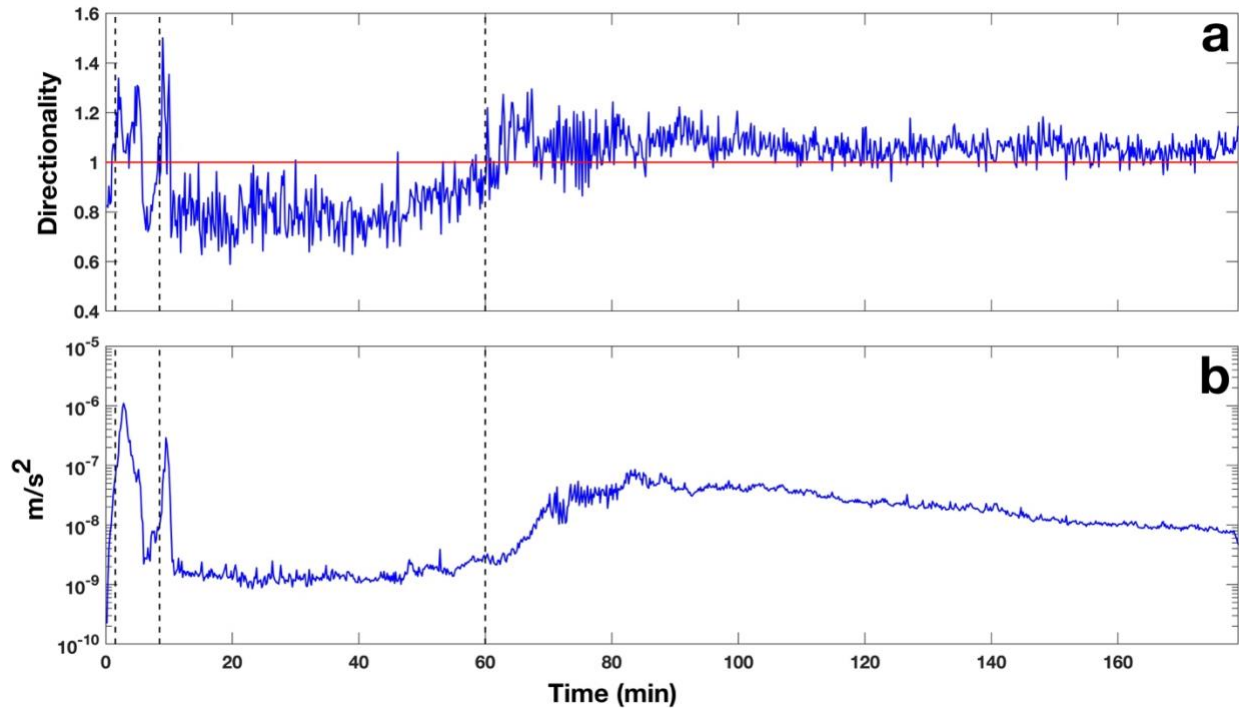
463 *Figure 9 Conceptual models for the 18 March 2007 lahar at each of the three monitoring stations along the*
 464 *Whangaehu channel depicting flow type and the estimated seismic properties at each flow phase. a) RTMT 7.4 km*
 465 *from source, b) TRAN 28 km from source, and c) COLL 83 km from source. Flow types (FT) are as followed;*
 466 *streamflow (SF), bow wave streamflow (BW), hyperconcentrated flow (HF), Transitional flow (TF), and sediment-*
 467 *laden streamflow (SLF). Note, decreased (D), increased (I), high (H), low (L), and mixed (M) are notations for*
 468 *directionality ratios and peak spectral frequency estimates.*

469 Another implication for future warning is the implementation of 3-component sensors and the
 470 use of DRs for channels that have streamflow. Walsh et al. (2020) showed for lahars flowing in
 471 La Lumbre channel at Volcán de Colima that the DR for streamflow is <1 and then increases
 472 when the lahar arrives. This same feature can be seen at each of the three monitoring sites for

473 the 18 March 2007 event (Figure 6) indicating differing flow types will still show this DR pattern
474 within the same flow and at other channels. To further show this, there were three natural non-
475 lake-breakout eruption-based lahars that occurred in the Whangaehu channel in September
476 2007 (for more details on the lahars see Cole et al., 2009; Kilgour et al., 2010) and recorded on
477 the seismometer at RTMT. The DR for the September events starts with streamflow with a DR <
478 1 and when the first lahar arrives the DR increases to >1 and as the lahar fully passes, the DR
479 decreases to <1 again (Figure 10a). As the second lahar arrives at RTMT (Figure 10, second
480 dashed line), the DR increases to >1 again. After the second lahar passes the DR decreases once
481 again back below DR<1. Finally, as the third lahar arrives (Figure 10, third dashed line) the DR
482 yet again increases above 1 for the entirety of the event.

483 For many mass flows and especially those that flow into channels with preexisting streamflow,
484 the peak seismic amplitude does not always coincide with the arrival of the mass flow, and thus
485 may not be the most reliable for event detection or warning. These observations may be due to
486 a frontal surge, the lag in sediment concentration or differences in peak amplitude with peak
487 discharge. Phase 1 (frontal streamflow surge) of the model proposed by Cronin et al. (1999) was
488 based on a hyperconcentrated flow interacting with streamflow, but has also been shown for
489 debris flows as well (e.g. Arratano and Moia, 1999). Arratano and Moia (1999) showed at
490 Moscardo Torrent, Italy, through a hydrograph that there was a precursory surge ahead of the
491 debris flow that was not seen in the seismic record. Similarly, at Ruapehu, for the 18 March
492 2007 lahar, at each of the three stations there is little evidence in the seismic amplitude that
493 there was a precursory surge or phase 1 (Figures 3-5, bottom panel). Conversely, the surge
494 ahead of the lahar can be seen in both the PSF analysis (drop to low frequencies) and in the DR

495 (decrease in DR) right before the peak seismic amplitude arrives. This shows that when
496 monitoring for future events that not only the amplitude should be used, but other analysis
497 (e.g. PSF, DR) as well, otherwise there could be a delay in the detection of an event.



498
499 *Figure 10 (a) Directionality ratio for the time sequence of the three lahars that occurred on 25 September 2007. (b)*
500 *RMS amplitude of the seismic record at RTMT during the timing of the three September lahars. Note that the black*
501 *dashed lines represent the timing of each lahar arriving at the monitoring site.*

502 Using all three components of the seismometer can be very beneficial in lahar monitoring. The
503 above-mentioned DR analysis can only be completed with horizontal recording, and analyzing
504 PSF in each component can yield critical information about the flow properties and dynamics.
505 Examining the seismic amplitude differences can generate significant discoveries, for example,
506 when the vertical component is stronger than the horizontal components, bedload dominates
507 over turbulence noise (Burtin et al., 2010). Greater flow parallel signals may indicate higher
508 water transport noises (Barrier et al., 2015) and higher cross-channel signals could be caused by

509 increased interflow particle collisions and flow-channel wall interactions (Doyle et al., 2010).
510 While using the differences in each component can be useful, there are also some concerns.
511 Channel geometry and bed conditions can alter the seismic signal (e.g. Coviello et al., 2019;
512 Marchetti et al., 2019). Additionally, the flow parallel direction can be influenced by the lahar
513 that has already passed, the lahar at the station and the lahar arriving. Furthermore, the tilt of
514 the seismometer may play a large role in determining which component is larger (e.g. Anthony
515 et al., 2018). In the case of the 18 March 2007 lahar a large pulse of water passed the stations
516 which may explain why the parallel component is stronger than the other two components at
517 RTMT and TRAN. At COLL, the lahar had elongated, lost energy, and thus shows more
518 decreased flow parallel energy compared to the previous two stations. In the cross-channel
519 direction, if a flow overtops the channel, the amplitude would presumably be dampened. This
520 may be the case at TRAN where both the flow parallel and vertical directions are more
521 energetic than the cross-channel amplitude after the passing of the head and breaking out of
522 the channel occurred (Figures 2d, 4 bottom row). Another concern when using the horizontal
523 components of a seismometer are the effects shallow layers may have on the site response of
524 the sensor. This is especially true when a sensor is installed on soft or loose sediment (e.g. soil,
525 fluvial/alluvial deposits). To test for potential effects by shallow layer fundamental frequencies,
526 H/V analysis of ambient noise (streamflow dominant) was conducted (see Supplementary
527 material). For RTMT, the H/V results depict a broad frequency peak between 5-15 Hz with a
528 local maximum at ~8 Hz (Figure S4a). Comparing the H/V frequency with the PSF of RTMT
529 (Figure 3), the only overlap is immediately before the front of the lahar passes the station
530 where the PSF decreases for ~1 minute before the head of the lahar arrives. The H/V analysis

531 for TRAN has a multi- broad-peak shape, with frequency peaks at ~14 and ~28-35 Hz (Figure
532 S4b). While these frequencies are similar to PSF values for TRAN (Figure 4), the H/V analysis has
533 no distinguishable fundamental frequency, contains large error, and no frequency peak has a
534 H/V amplification > 2 . In order for a H/V frequency peak to be considered ideal, generally the
535 amplification must to be greater than 2 and the standard deviation lower than a factor of 2
536 (SESAME, 2004). The H/V amplification for COLL displays a broad frequency peak between 13-
537 18 Hz, with a local maximum at ~18 Hz (Figure S4c). Comparing the PSFs at COLL (Figure 5), only
538 the cross-channel direction has significant PSF values in the same frequency range (~18 Hz
539 band). With all three stations not yielding distinct H/V frequency peaks, we surmise that the
540 PSF content for the 18 March 2007 lake-breakout lahar is most likely dominated by the large
541 flow passing by the seismic sensor rather than large site amplification effects from a shallow
542 layer. While this may be the case, there is still the possibility that some of the PSF values could
543 be due to local effects and should not be considered in the lahar analysis, e.g., the low PSFs at
544 RTMT between 15-20 min (Figure 3), at TRAN contributing to some of the “jumping” in PSF
545 content (Figure 4), or in the mostly dominant 15-20 Hz PSF in the cross-channel direction at
546 COLL. Conversely, SCF values at each station do not reside in the broad H/V frequency range at
547 any station (Figure 7), which may further support the hypothesis that almost all of the recorded
548 frequencies are indeed produced by the lahar. With the use of horizontal components
549 becoming common in mass flow monitoring, future 3-component analyses of mass flows should
550 consider estimating H/V ratios or use other site response methods (e.g. spectral ratio analysis)
551 in order to identify whether near-surface structures may affect the recorded flow data. Overall,
552 all these concerns can and should be tested to estimate potential error in 3-component

553 methods. Nevertheless, using all three components of the seismometer can enhance the
554 productivity of warning systems, and if possible, should be used instead of single component
555 sensors.

556 **5. Conclusions**

557 At 23:18 UTC on 18 March 2007 Mt. Ruapehu produced the biggest lahar in New Zealand in
558 over 100 years causing $1.3 \times 10^6 \text{ m}^3$ of water to flow out of the Crater Lake and rush down the
559 Whangaehu channel flowing for over 200 km to the Tasman sea. Seismic analysis at three
560 monitoring locations along the channel (7.4, 28, and 83 km) yielded an understanding of how
561 flow type and processes of the lahar evolve with distance. The proximal lahar was a highly
562 turbulent outburst flood, which generated high PSF content in all three components. Further
563 along the channel after the lahar had bulked up and transformed into a multi-phase
564 hyperconcentrated flow, the PSF content was variable and showed changes in the flow
565 regime/phase. Finally, at the most distal monitoring station, the lahar had lost energy and
566 transformed into a slurry-type flow where the PSF content became more bedload-dominant.
567 Additionally, directionality ratios from all three sites along with data from additional lahars
568 yielded strong evidence that DRs can be used for warning systems when there is streamflow
569 present in the channel. Furthermore, PSF and DRs show evidence of a pre-lahar water pulse
570 that is concealed in the raw seismic data, but has been observed visually. Ultimately, the use of
571 3-component broadband seismic analysis for the 18 March 2007 lahar at Mt. Ruapehu may lead
572 to more accurate and advanced real-time warning systems for mass flows through the use of
573 frequency and directionality around the world.

574 *Author Contribution*

575 BW performed seismic analysis and drafted the manuscript, CL organized and prepared data,
576 and JP created the visual location representation of the event. All participating authors
577 contributed to the discussions and editing of the draft of the manuscript, as well as approving
578 the final edition.

579 *Competing Interests*

580 The authors declare that they have no conflict of interest

581 *Acknowledgements*

582 This work was supported by the Resilience to Natures Challenges – New Zealand National
583 Science, volcano program of research. We would also like to thank all the people from Massey
584 University, Horizons Regional Council, NIWA, and the Department of Conservation that
585 collected data and set up monitoring locations all along the channel in preparation for and
586 during the lahar. A final special thanks to Kate Arentsen for editorial support.

587 **References**

588 Anthony, R., Aster, R., Ryan, S., Rathburn, S., Baker, M.: Measuring mountain river discharge
589 using seismographs emplaced within the hyporheic zone, *Journal of Geophysical Research:*
590 *Earth Surface*, 123, 210-228, 2018.

591 Arattano, M., Marchi, L.: Measurements of debris flow velocity trough cross-correlation of
592 instrumentation data, *Natural Hazards and Earth System Sciences*, 5, 137-142, 2005.

593 Arattano, M., Moia, F.: Monitoring the propagation of debris flow along a torrent, *Hydrological*
594 *Sciences- Journal des Sciences Hydrologiques*, 44(5), 811-823, 1999.

595 Barriere, J., Oth, A., Hostache, R., Krein, A.: Bed load transport monitoring using seismic
596 observations in a low-gradient rural gravel bed stream, *Geophys. Res. Lett.*, 42, 2294-2301,
597 2015.

598 Bartholomaus, T., Amundson, J., Walter, J., O'Neel, S., West, M., Larsen, C.: Subglacial discharge
599 at tidewater glaciers revealed by seismic tremor, *Geophys. Res. Lett.*, 42, 6391-6398, 2015.

600 Burtin, A., Vergne, J., Rivera, L., Dubernet, P.: Location of river-induced seismic signal from
601 noise correlation functions, *Geophys. J. Int.*, 182, 1161-1173, 2010.

602 Capra, L., Borselli, L., Barley, N., Ruiz, J., Norini, G., Sarocchi, D., Caballero, L., Cortes, A.:
603 Rainfall-triggered lahars at Volcan de Colima, Mexico: Surface hydro-repellency as initiation
604 process, *Journal of Volcanology and Geothermal Research*, 198, 105-117, 2010.

605 Capra, L., Coviello, V., Borselli, L., Marquez-Ramirez, V., Arambula-Mendoza, R.: Hydrological
606 control of large hurricane-induced lahars: evidence from rainfall-runoff modeling, seismic and
607 video monitoring, *Nat. Hazards Earth Syst. Sci.*, 18, 781-794, 2018.

608 Carrivick, J., Manville, V.: A fluid dynamics approach to modelling the 18th March 2007 lahar at
609 Mt. Ruapehu, New Zealand, *Bull. Volcanol.*, 71, 153-169, 2009.

610 Cole, S., Cronin, S., Sherburn, S., Manville, V.: Seismic signals of snow-slurry lahars in motion: 25
611 September 2007, Mt Ruapehu, New Zealand, *Geophys. Res. Lett.*, 36, L09405, 2009.

612 Coviello, V., Arattano, M., Comiti, F., Macconi, P., Marchi, L.: Seismic characterization of debris
613 flows: Insights into energy radiation and implications for warning, *Journal of Geophysical*
614 *Research: Earth Surface*, 124, 2019.

615 Coviello, V., Capra, L., Vazquez, R., Marquez-Ramirez, V.: Seismic characterization of
616 hyperconcentrated flows in a volcanic environment, *Earth Surf. Process. Landforms.*, 43, 2219-
617 2231, 2018.

618 Cronin, S., Neall, V., Jerome, L., Palmer, A.: Unusual “snow slurry” lahars from Ruapehu volcano,
619 New Zealand, September 1995, *Geology*, 24, 1107-1110, 1996.

620 Cronin, S., Neall, V., Jerome, L., Palmer, A.: Dynamic interactions between lahars and stream
621 flow: A case study from Ruapehu volcano, New Zealand, *GSA Bulletin*, 111(1), 28-38, 1999.

622 Cronin, S., Neall, V., Jerome, L., Palmer, A.: Transformation, internal stratification, and
623 depositional processes within a channelized, multi-peaked lahar flow, *New Zealand Journal of*
624 *Geology and Geophysics*, 43, 117-128, 2000.

625 Doyle, E., Cronin, S., Cole, S., Thouret, J.: The coalescence and organization of lahars at Semeru
626 volcano, Indonesia, *Bull. Volcanol.*, 72, 961-970, 2010.

627 Doyle, E., Cronin, S., Cole, S., Thouret, J.: Defining conditions for bulking and debulking in
628 lahars, *GSA Bulletin*, 123, 1234-1246, 2011.

629 Huang, C., Shieh, C., Yin, H.: Laboratory study of the underground sound generated by debris
630 flows, *Journal of Geophysical Research*, 109, F01008, 2004.

631 Iguchi, M.: Proposal of estimation method for debris flow potential considering eruptive
632 activity, *Journal of Disaster Research*, 14(1), 126-134, 2019.

633 Gimbert, F., Tsai, V., Lamb, M.: A physical model for seismic noise generation by turbulent flow
634 in rivers, *Journal of Geophysical Research: Earth Surface*, 119, 2209-2238, 2014.

635 Keys, H., Green, P.: Ruapehu lahar New Zealand 18 March 2007: Lessons for hazard assessment
636 and risk mitigation 1995-2007, *Journal of Disaster Research*, 3(4), 284-296, 2008.

637 Kilgour, G., Manville, V., Della Pasqua, F., Graettinger, A., Hodgson, K., Joly, G.: The 25
638 September 2007 eruption of Mount Ruapehu, New Zealand: Directed ballistics, surtseyan jets,
639 and ice-slurry lahars, *Journal of Volcanology and Geothermal Research*, 191, 1-14, 2010.

640 Kogelnig, A., Surinach, E., Vilajosana, I., Hubl, J., Sovilla, B., Hiller, M., Dufour, F.: On the
641 complementariness of infrasound and seismic sensors for monitoring snow avalanches, *Nat.*
642 *Hazards Earth Syst. Sci.*, 11, 2355-2370, 2011.

643 Kuehnert, J., Mangeney, A., Capdeville, Y., Vilotte, J., Stutzmann, E., Chaljub, E., et al.: Locating
644 rockfalls using inter-station ratios of seismic energy at Dolomieu crater, Piton de la Fournaise
645 volcano, *Journal of Geophysical Research: Earth Surface*, 126, e2020JF005715, 2021.

646 Lube, G., Cronin, S., Manville, V., Procter, J., Cole, S., Freundt, A.: *Geology*, 40, 475-478, 2012.

647 Manville, V., Cronin, S.: Breakout lahar from New Zealand's crater lake, *EOS Transactions*,
648 88(43), 441-456, 2007.

649 Manville, V., White, J., Hodgson, K.: Dynamic interactions between lahars and stream flow: A
650 case study from Ruapehu volcano, New Zealand: Discussion and reply discussion, *GSA Bulletin*,
651 *112(7)*, 1149-1152, 2000.

652 Marchetti, E., Walter, F., Barfucci, G., Genco, R., Wenner, M., Ripepe, M., McArdell, B., Price, C.:
653 Infrasound array analysis of debris flow activity and implications for early warning, *Journal of*
654 *Geophysical Research: Earth Surface*, *124*, 567-587, 2019.

655 Massey, C., Manville, V., Hancox, G., Keys, H., Lawrence, C., McSaveney, M.: Out-burst flood
656 (lahar) triggered by retrogressive landsliding, 18 March 2007 at Mt Ruapehu, New Zealand – a
657 successful early warning, *Landslides*, *7*, 303-315, 2010.

658 O'Connor, J., Clague, J., Walder, J., Manville, V., Beebe, R.: Outburst Floods, *Reference Module*
659 *in Earth Systems and Environmental Sciences*, Elsevier, 2020.

660 O'Shea, B.: Ruapehu and the Tangiwai disaster, *NZ J. Sci. Tech.* *36B*, 174-189, 1954.

661 Pardo, N., Cronin, S., Palmer, A., Nemeth, K.: Reconstructing the largest explosive eruptions of
662 Mt. Ruapehu, New Zealand: Lithostratigraphic tools to understand subplinian-plinian eruptions
663 at andesitic volcanoes, *Bull. Volcanol.*, *74*, 617-640, 2012.

664 Pierson, T., Janda, R., Thouret, J., Borrero, C.: Perturbation and melting of snow and ice by the
665 13 November 1985 eruption of Nevado del Ruiz, Colombia, and consequent mobilization, flow
666 and deposition of lahars, *J. Volcanol. Geotherm. Res.*, *41(1)*, 17-66, 1990.

667 Pierson, T., Scott, K.: Downstream dilution of a lahar: Transition from debris flow to
668 hyperconcentrated streamflow, *Water Resources Research*, *21(10)*, 1511-1524, 1985.

669 Procter, J., Cronin, S., Fuller, I., Lube, G., Manville, V.: Quantifying the geomorphic impacts of a
670 lake-breakout lahar, Mount Ruapehu, New Zealand, *Geology*, 38, 67-70, 2010.

671 Procter, J., Cronin, S., Sheridan, M.: Evaluation of Titan2D modelling forecasts for the 2007
672 Crater Lake break-out lahar, Mt. Ruapehu, New Zealand, *Geomorphology*, 136, 95-105, 2012.

673 Procter, J., Cronin, S., Fuller, I., Sheridan, M., Neall, V., Keys, H.: Lahar hazard assessment using
674 Titan2D for an alluvial fan with rapidly changing geomorphology: Whangaehu River, Mt.
675 Ruapehu, *Geomorphology*, 116, 162-174, 2010.

676 Procter, J. N., Cronin, S. J., Zernack, A. V., Lube, G., Stewart, R. B., Nemeth, K., & Keys, H.: Debris
677 flow evolution and the activation of an explosive hydrothermal system; Te Maari, Tongariro,
678 New Zealand. *Journal of Volcanology and Geothermal Research*, 286, 303-316, 2014.

679 Procter, J., Zernack, A., Mead, S., Morgan, M., & Cronin, S.: A review of lahars; past deposits,
680 historic events and present-day simulations from Mt. Ruapehu and Mt. Taranaki, New
681 Zealand. *New Zealand Journal of Geology and Geophysics*, 64(2-3), 479-503, 2021.

682 Roth, D., Brodsky, E., Finnegan, N., Rickenmann, D., Turowski, J., Badoux, A.: Bed load sediment
683 transport inferred from seismic signals near a river, *J. Geophys. Res. Earth Surf.*, 121, 725-747,
684 2016.

685 Schimmel, A., Coviello, V., Comiti, F.: Debris-flow velocity and volume estimations based on
686 seismic data, *Natural Hazards and Earth System Sciences*, 2021.

687 Schmandt, B., Aster, R., Scherler, D., Tsai, V., Karlstrom, K.: Multiple fluvial processes detected
688 by river side seismic and infrasound monitoring of a controlled floor in the Grand Canyon,
689 *Geophys. Res. Lett.*, 40(18), 4858-4863, 2013.

690 Schmandt, B., Gaeuman, D., Stewart, R., Hansen, S., Tsai, V., Smith, J.: Seismic array constraints
691 on reach-scale bedload transport, *Geology*, 45, 299-302, 2017.

692 Saló, L., Corminas, J., Lantada, N., Mata, G., Prades, A., Ruiz-Carulla, R.: Seismic energy analysis
693 as generated by impact and fragmentation of single-block experimental rockfalls, *Journal of*
694 *Geophysical Research: Earth Surface*, 123, 1450-1478, 2018.

695 Scott, K.: Origins, behavior, and sedimentology of lahars and lahar runout flows in the Toutle-
696 Cowlitz river system, *USGS Professional Paper*, 1988.

697 Surinach, E., Vilajosana, I., Khazaradze, G., Biescas, B., Furdada, G., Vilaplana, J.: Seismic
698 detection and characterization of landslides and other mass movements, *Natural Hazards and*
699 *Earth System Sciences*, 5, 791-798, 2005.

700 Walsh, B., Coviello, V., Capra, L., Procter, J., Marquez-Ramirez, V.: Insights into the internal
701 dynamics of natural lahars from analysis of 3-component broadband seismic signals at Volcán
702 de Colima, Mexico, *Front. Earth Sci.* 8, 542116, 2020.

703 Walsh, B., Jolly, A., Procter, J.: Seismic analysis of the 13 October 2012 Te Maari, New Zealand,
704 lake breakout lahar: Insights into flow dynamics and the implications on mass flow monitoring,
705 *J. Volcanol. Geotherm. Res.*, 324,144-155, 2016.